

Synchronizing Bloch-oscillating free carriers in moiré flat bands

Ali Fahimniya¹, Zhiyu Dong¹, Egor I. Kiselev², Leonid Levitov¹

¹*Physics Department, Massachusetts Institute of Technology, Cambridge, Massachusetts 02139, USA*

²*Institut für Theorie der Kondensierten Materie,
Karlsruher Institut für Technologie, 76131 Karlsruhe, Germany*

Achieving Bloch oscillations of free carriers under a direct current, a long-sought-after collective many-body behavior, has been challenging due to stringent constraints on the band properties. We argue that the flat bands in moiré graphene fulfill the basic requirements for observing Bloch oscillations, offering an appealing alternative to the stacked quantum wells used in previous work aiming to access this regime. Bloch-oscillating moiré superlattices emit a comb-like spectrum of incommensurate frequencies, a property of interest for converting direct currents into high-frequency currents and developing broad-band amplifiers in THz domain. The oscillations can be synchronized through coupling to an oscillator mode in a photonic or plasmonic resonator. Phase-coherent collective oscillations in the resonant regime provide a realization of current-pumped THz lasing.

Bloch oscillations, arising when electrons are driven through a perfect crystal lattice by an electric field, are an iconic example of a coherent dynamics in quantum many-body systems[1, 2]. The oscillations are at the same frequency for all carriers, for a one-dimensional lattice given by $\omega = eEa/\hbar$ with E the field strength and a the lattice period. Besides the obvious fundamental appeal, this behavior has long been eyed as a promising way to convert direct currents into high-frequency currents[3]. Wide interest in this phenomenon stems from the expectation that it may help fill the infamous “THz gap”, leading to radiation emitters and detectors operating in this frequency range[4–6].

While Bloch oscillations have long been immortalized in textbooks, realizing them in solids has proven to be a challenging task. Achieving this regime requires overcoming several obstacles. One is the dephasing due to electron energy loss to phonons. To suppress phonon emission exceptionally narrow electronic bands of width smaller than the optical phonon energy must be used. Another is the dephasing due to disorder scattering. Experimental efforts so far mainly focused on narrow minibands in synthetic MBE-grown semiconductor superlattices[6–9]. These systems cleared a number of key milestones on the road towards achieving Bloch oscillations. They display the signatures indicative of Bloch oscillations such as negative differential conductivity $dI/dV < 0$, recurrence and ringing in the optical pump-probe measurements, Wannier-Stark (WS) ladders and, last but not least, optical gain[6–9]. However, upon the injection current approaching the relevant parameter range the superlattice systems develop instabilities and show a complex noisy behavior due to the onset of switching and formation of electric domains. This behavior presents the main obstacle to achieving the collective globally-synchronized Bloch oscillations[11–13].

Meanwhile, recently Bloch oscillations were achieved in cold atom systems, using Bloch minibands in optical lattices[14–18]. This proof-of-principle demonstration has greatly improved our understanding of the underlying physics[19, 22] and strengthened interest in demonstrating electronic Bloch oscillations.

Given the difficulties encountered in semiconducting superlattices it is natural to seek other systems that meet the requirements for achieving Bloch oscillations. One enticing opportunity is offered by the recently introduced moiré superlattices in twisted bilayer graphene, a material that hosts electron bands that are tunable by the twist angle[23–28]. For twist angles $\theta \lesssim 2^\circ$ the moiré electron bands are considerably narrower than the optical phonon energy (~ 200 meV), becoming as narrow as $J \lesssim 10$ -20 meV near “magic” values of the twist angle $\theta \sim 1^\circ$. Such bandwidths are sufficient to eliminate the optical phonon emission, the main obstacle to observing coherent Bloch oscillations in wide bands.

The moiré graphene also clears other key requirements for observing Bloch oscillations. One is weak disorder scattering. Since the narrow bands are formed in a solid with a pristine near-perfect atomic order, they are less susceptible to disorder than the bands in synthetic MBE-grown semiconductor superlattices. This is manifested in a high carrier mobility and ballistic carrier transport observed over micron lengthscales at $T = 0$ [27, 28]. Estimating the scattering time as $\tau = l/v_F$ with the mean free path $l \sim 1 \mu\text{m}$ and velocity v_F of about 1/30 of the graphene monolayer value 10^6 m/s gives $\tau \sim 3 \cdot 10^{-11}$ s, a value comparable to that of graphene monolayer. The scattering rate can therefore be as low as $\gamma_{\text{dis}} \sim 10^{-2} J$. The two-dimensional character of moiré graphene will also help to suppress the instability towards the formation of electric field domains that hindered experiments in the stacks of quantum wells[6]. In the moiré setup the electric current can be driven in the graphene plane in a manner that maintains the translation invariance of the system and does not cause local charging. Indeed, gating is known to maintain a spatially uniform carrier density even under moderate to high currents.

Other appealing properties of moiré graphene are the lack of Zener transitions, suppressed by sizable minigaps, and the weakness of the electron coupling to the long-wavelength acoustic phonons[29–31]. Further, the relatively large periodicity of moiré superlattices ($a \sim 10$ nm)

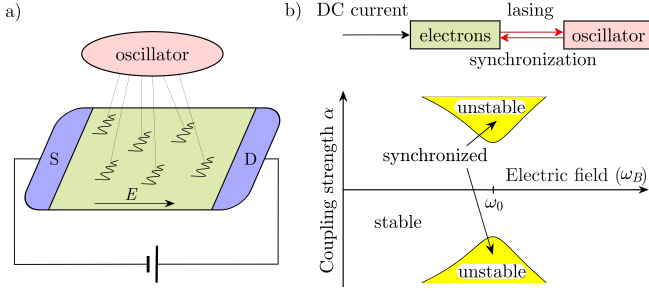


FIG. 1: a) Bloch-oscillating electrons synchronized by coupling to an oscillator mode. A DC electric field \mathbf{E} drives free-carrier oscillations with frequency ω_B (wavy lines). The oscillations are at the same frequency for all carriers but are asynchronous (not in phase). Synchronized oscillations are achieved through coupling to an oscillator mode, depicted by the thin lines. b) A phase diagram showing the stable and unstable regimes, in which Bloch oscillations are asynchronous and synchronized, respectively. The carrier scattering rate γ is taken to be equal the oscillator damping γ_0 (see Eq.(11)); phase diagrams for unequal γ and γ_0 are discussed in [37]. The Bloch frequency ω_B on the x axis is proportional to the electric field; ω_0 is the oscillator frequency, the coupling strength α between electrons and the oscillator is defined in Eq.(9). Instability is easiest to achieve when ω_B is tuned close to ω_0 . The flowchart on top shows the relationship between different degrees of freedom: the DC current drives free-carrier oscillations; these, synchronized by the oscillator, pump energy into it (the lasing effect).

reduces the required E field values:

$$\gamma = \max[\gamma_{\text{ph}}, \gamma_{\text{dis}}] < \omega_B < J/\hbar, \quad \omega_B = eEa/\hbar. \quad (1)$$

Using moderate E fields will help to avoid the WS localization effects and charge instabilities.

A key assumption is that phonon emission can remain relatively weak despite rate enhancement due to the high density of states in moiré bands and an out-of-equilibrium carrier state created under an applied current. These expectations are supported by a detailed analysis of phonon emission[37], predicting emission rates which drop upon an increase in the flat-band width and a growing E field. Detuning away from the magic twist angle reduces the density of states that govern phonon emission. Likewise, an E field tunes the WS states out of resonance, abruptly quenching phonon emission.

Importantly, although all free carriers Bloch-oscillate with identical frequencies, these oscillations are *asynchronous*, as the oscillation phases are totally random and uncorrelated for different carriers. Therefore, in order to achieve collective continuous-wave Bloch oscillations driven by a direct current, movements of different carriers must be synchronized. We outline a way to achieve this through coupling of the current-carrying channel to an oscillator mode in a THz resonator. The resonator frequency depends on system parameters, whereas the Bloch frequency is tunable by varying the applied electric field. As illustrated in Fig.1,

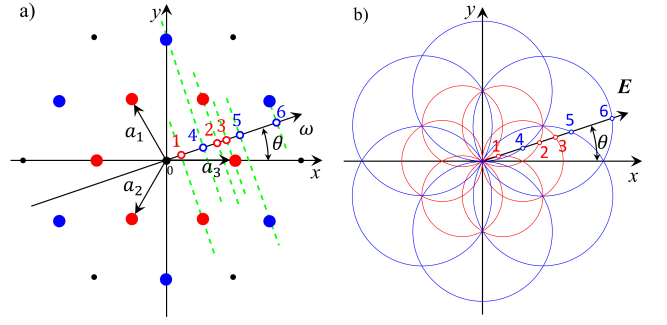


FIG. 2: a) Geometric construction of the frequency comb for Bloch oscillations, Eq.(2), at a generic electric field orientation. Frequencies ω_l are found by projecting the real-space Bravais lattice points (solid circles) onto the 1D line parallel to \mathbf{E} (black arrow) as indicated by dashed green lines. The shortest and next-shortest vectors are shown as red and blue dots. Hollow circles, found by projection, give the frequencies in Eq.(2), where the emitted noise power $P(\omega)$ peaks. b) Visualization of the comb ω_l angle dependence vs. \mathbf{E} orientation relative to the superlattice.

this system develops an instability towards collective oscillations at a Bloch frequency when the latter is close to the oscillator frequency. In practice, the oscillator can be realized as a THz photonic or plasmonic resonator in a 2D or a 3D architecture[6, 32–36]. An alternative route to achieve synchronization is through coupling to an intrinsic collective mode, excitonic or plasmonic. Phase-coherent oscillations achieved in this regime represent a realization of electrically pumped THz lasing.

Before discussing the synchronization problem we summarize the basic picture of the free-carrier Bloch oscillations in superlattices. In superlattices of dimension $D \geq 2$ different carriers can move at different angles relative to the applied field[10, 19–22]. Nevertheless, the main properties of the one-dimensional Bloch oscillations persist. The Bloch frequencies remain discrete, taking values identical for all carriers in the system. A new aspect is that different harmonics of the band dispersion produce oscillations with several different discrete frequencies. These frequencies are in general incommensurate with one another, forming a comb-like spectrum pictured in Figs.2 and 3.

The frequency comb dependence on the electric field orientation is described by the geometric construction illustrated in Fig.2. Namely, possible frequencies are given by the projections of different Bravais lattice vectors $\mathbf{a}_l = n_1 \mathbf{a}_1^{(0)} + n_2 \mathbf{a}_2^{(0)}$ on the applied field \mathbf{E} :

$$\omega_l = \frac{e}{\hbar} \mathbf{E} \cdot \mathbf{a}_l = \frac{e}{\hbar} E a_l \cos(\theta - \theta_l) \quad (2)$$

The dependence of the frequencies ω_l on the field \mathbf{E} orientation and strength, as well as the tunability of moiré superlattices by the twist angle, provide knobs that will facilitate achieving Bloch oscillations in moiré graphene.

This result can be illustrated by considering a general

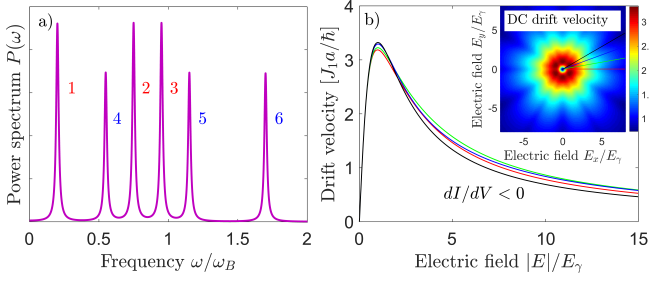


FIG. 3: a) The comblike frequency spectrum of current fluctuations, Eq.(5), consisting of finite-width resonances at the discrete frequency values ω_l , Eq.(2). Frequency units are $\omega_B = \frac{e}{\hbar} E a$, the power spectrum $P(\omega)$ is in arbitrary units. The field orientation and labeling of different peaks match those in Fig.2. b) The direct-current drift velocity, Eq.(6). Shown is the full dependence (inset) and traces for several different field orientations. Bloch oscillations occur for field strength $E > E_\gamma = \hbar\gamma/ea$; negative differential conductivity $dI/dV < 0$ is a hallmark of this regime.

tight binding band on a monoatomic lattice,

$$\epsilon(\mathbf{k}) = \sum_{l=1,2,\dots} -2J_l \cos(\mathbf{k} \cdot \mathbf{a}_l). \quad (3)$$

The Bravais lattice vectors \mathbf{a}_l describe hopping between different pairs of lattice sites, either nearest-neighbor or non-nearest-neighbor. Bloch-oscillating free carriers obey quasiclassical equations of motion

$$\hbar \frac{d\mathbf{k}}{dt} = e\mathbf{E}, \quad (4)$$

generating a linear time dependence $\mathbf{k}(t) = \frac{e}{\hbar} \mathbf{E}t + \mathbf{k}_0$ with the linear part identical for all carriers and a carrier-specific initial value \mathbf{k}_0 . With this bandstructure and an electric field of a generic orientation, $\mathbf{E} = E(\cos\theta, \sin\theta)$, the frequencies at which the time-dependent velocity of the electrons $\mathbf{v}(t) = \frac{1}{\hbar} \nabla_{\mathbf{k}} \epsilon(\mathbf{k})|_{\mathbf{k}=\frac{e}{\hbar} \mathbf{E}t + \mathbf{k}_0}$ will oscillate are given by \mathbf{a}_l projected on \mathbf{E} , Eq.(2). The resulting dependence of the frequencies ω_l on the orientation of \mathbf{E} is described by families of circles pictured in Fig.2.

Physically, discrete frequency values arise because electron trajectories sweep the (reduced) Brillouin zone (BZ) of a two-dimensional crystal in the direction set by the \mathbf{E} vector. Every time an electron reaches zone boundary it umklapps to the opposite side and continues forward, winding around the BZ at different frequencies in different crystal axes directions. In that, the time-averaged rate of winding around BZ along the direction of \mathbf{E} is the same for all carriers. This leads, for a general field orientation, to a quasiperiodic dynamics characterized by two fundamental frequencies which depend only on the field \mathbf{E} and lattice periodicity as described in Eq.(2), wherein $\omega_l = n_1\omega_1 + n_2\omega_2$ in agreement with the geometric construction in Fig.2.

In the presence of momentum-relaxing scattering the frequency spectrum broadens into a sum of finite-width

resonances centered at $\omega = \omega_l$. The quantity of interest is the autocorrelation function of current fluctuations $P(\omega) = \frac{1}{2} \int_{-\infty}^{\infty} \langle \delta \mathbf{j}(t) \cdot \delta \mathbf{j}(t + \tau) \rangle e^{-i\omega\tau} d\tau$ which describes the spectrum of electric noise emitted by the system. Simple analysis predicts a comb-like emitted power spectrum

$$P(\omega) = \sum_l \frac{P_l}{(\omega - \omega_l)^2 + \gamma^2} \quad (5)$$

(see [37]). The Bloch oscillation regime corresponds to non-overlapping resonances. Since the frequencies ω_l are proportional to the applied field \mathbf{E} the oscillations appear when the field strength exceeds a threshold set by momentum-relaxing scattering, $E_\gamma = \hbar\gamma/ea$. At lower fields the resonances merge into a broadband noise spectrum, indicating a suppression of the oscillations.

In the Bloch oscillation regime the DC drift velocity exhibits negative differential conductivity $dI/dV < 0$, a characteristic behavior that provides a clear signature of this regime. A direct calculation [37] predicts

$$v_{DC} = \sum_l \mathbf{a}_l \frac{2J_l f_l}{\hbar} \frac{\gamma\omega_l}{\gamma^2 + \omega_l^2}, \quad f_l = \sum_k f_0(k) e^{i\mathbf{a}_l \cdot \mathbf{k}}, \quad (6)$$

with $f_0(k)$ the steady-state momentum distribution. The dependence on the field E is linear at small $E < E_\gamma$ and falls off as $1/E$ at large $E > E_\gamma$. Interestingly, current depends on the dimensionless quantity E/E_γ in a way that is independent of the specific value of γ . This behavior is illustrated in Fig.3(b). The drift velocity for electric fields in different directions is shown in the inset.

Next, we turn to the discussion of Bloch oscillations synchronized by coupling to an external oscillator mode:

$$H = \sum_i [\epsilon(\mathbf{p}_i) - e\mathbf{E}\mathbf{x}_i - \alpha Q\mathbf{x}_i] + \frac{1}{2m} P^2 + \frac{\omega_0^2 m}{2} Q^2. \quad (7)$$

Here $\epsilon(\mathbf{p})$ is the band dispersion, \mathbf{p}_i and \mathbf{x}_i are the momenta and coordinates of the electrons; P and Q are the momentum and amplitude of the oscillator. The Bloch electron coupling to the oscillator and the external field is through potentials $U(\mathbf{x}_i) = -e\mathbf{E}\mathbf{x}_i - \alpha Q\mathbf{x}_i$ seen by each of the electrons. In this approach we ignore the direct carrier-carrier interactions, treating electron dynamics in a free-particle approximation. Bloch oscillations are driven by the electric field E , the term $-\alpha Q\mathbf{x}_i$ describes coupling of the electrons to the oscillator mode. In practice the oscillator can be realized as e.g. THz photonic or plasmonic resonators[6, 32–36].

Starting from the equations of motion originating from the Hamiltonian above, we wish to integrate out the carrier degrees of freedom and derive a closed-form dynamics for the oscillator. For that purpose we solve equations of motion for the i -th electron beginning from the time $t'_i < t$ when its state was last reset by scattering and the Hamiltonian dynamics described by Eq.(7) had started.

The full set of equations of motion for the electrons and the oscillator is

$$\begin{aligned} \dot{\mathbf{p}}_i &= -\frac{\partial H}{\partial \mathbf{x}_i} = e\mathbf{E} + \alpha Q(t), \quad \dot{\mathbf{x}}_i = \frac{\partial H}{\partial \mathbf{p}_i} = \frac{\partial \epsilon(\mathbf{p}_i)}{\partial \mathbf{p}_i} \quad (8) \\ \dot{P} &= -m\omega_0^2 Q + \sum_i \alpha x_i, \quad \dot{Q} = P/m. \end{aligned}$$

Eliminating $P(t)$ yields a second-order equation of motion for the oscillator mode $Q(t)$, driven by an external force given by a sum of contributions due to the electrons

$$\ddot{Q}(t) + \omega_0^2 Q(t) = f(t), \quad f(t) = \frac{\alpha}{m} \sum_i x_i(t). \quad (9)$$

Importantly, the cumulative effect due to the electrons, given by the quantity $f(t)$, gives rise to a “memory effect” in the oscillator dynamics. Each term in the sum $\sum_i x_i(t)$ is given by a solution of the equations of motion for $x_i(t)$ and $p_i(t)$, Eq.(8), initialized at an earlier random time $t'_i < t$. The oscillator dynamics $Q(t)$, $P(t)$ during the time intervals $t'_i < \tau < t$ affects the electron states $x_i(t)$, $p_i(t)$, giving rise to a back-action $f(t) = \frac{\alpha}{m} \sum_i x_i(t)$ with the dynamical memory originating from the dependence on $Q(\tau)$ and $P(\tau)$ at the earlier times $\tau < t$.

The feedback due to this memory effect enables synchronization of Bloch dynamics, resulting in a macroscopic oscillating current generated by Bloch-oscillating electrons. To describe the instability we compute the backaction term linearized in $Q(t')$ (the analysis is lengthy but straightforward, see [37]). Substituting the result in Eq.(9) gives a characteristic equation for ω of the form

$$\omega_0^2 - \omega^2 = \frac{i\lambda}{\omega} \left(\frac{\gamma^2}{(\gamma^2 + \omega_B^2)(\gamma - i\omega)} + \frac{\gamma}{(\omega + i\gamma)^2 - \omega_B^2} \right), \quad (10)$$

where we defined $\lambda = N \frac{\alpha^2 a v_0}{m \hbar}$ with N the total number of Bloch-oscillating electrons.

The system becomes unstable when Eq.(10) admits solutions in the upper halfplane of complex ω . Before exploring this instability we inspect, as a sanity check, the regime of highly damped Bloch oscillations, $\gamma \gg \omega_B, \omega_0$. In this case, Eq.(10) reads $\omega_0^2 - \omega^2 = \frac{i\lambda}{\omega\gamma}$. At large γ , the roots of this equation are close to $\pm\omega_0$. Writing $\omega = \pm\omega_0 + \Delta\omega$, at leading order in $1/\gamma$ we find $\Delta\omega = -\frac{i\lambda}{2\omega_0^2\gamma}$. Negative imaginary part indicates that no instability arises in this regime, i.e. the driven system is stabilized by high damping.

A very different situation occurs at weak damping $\gamma \ll \omega_B, \omega_0$. The new behavior is simplest to understand close to the resonance between the oscillator and Bloch frequencies, $\omega_0 \approx \omega_B$. For ω values near the resonance, where the last term in Eq.(10) dominates, we can ignore the first non-resonant term. This gives

$$(\omega_0^2 - (\omega + i\gamma_0)^2)((\omega + i\gamma)^2 - \omega_B^2) = \frac{i\lambda\gamma}{\omega}. \quad (11)$$

Here we added the oscillator damping rate γ_0 . Working near the resonance and expanding in a small $\delta\omega = \omega - \omega_0 \ll \omega_0 \approx \omega_B$ to obtain the complex frequency roots positioned near ω_0 , the characteristic equation becomes

$$(\omega - \omega_0 + i\gamma_0)(\omega + i\gamma - \omega_B) = -i\eta/4, \quad \eta = \frac{\lambda\gamma}{\omega_0^3}. \quad (12)$$

The properties of Eq.(12) are particularly straightforward when $\gamma_0 = \gamma$. In this case, the roots are

$$\omega_{1,2} = -i\gamma + \frac{\omega_B + \omega_0 \pm \sqrt{(\omega_B - \omega_0)^2 - i\eta}}{2} \quad (13)$$

The system is stable if $\text{Im } \omega_{1,2} < 0$ and unstable otherwise. Using the identity

$$\text{Im} \left(\sqrt{x - i\eta} \right) = -\text{sgn } \eta \sqrt{\frac{\sqrt{x^2 + \eta^2} - x}{2}} \quad (14)$$

with $x = (\omega_B - \omega_0)^2$, the condition for the instability becomes

$$\eta^2 > ((\omega_B - \omega_0)^2 + 4\gamma^2) 16\gamma^2. \quad (15)$$

This criterion predicts the Bloch frequency ω_B and the coupling strength λ values for which an instability towards a synchronized dynamics may occur, giving the phase diagram shown in Fig.1. As expected on general grounds, the instability is easiest to achieve when Bloch oscillations are in resonance with the oscillator, $\omega_B = \omega_0$. Tuning away from the resonance suppresses the instability. The instability signals the onset of a collective regime in which Bloch-oscillating electrons become synchronized through coupling to the oscillator mode.

A wider variety of collective regimes can be achieved by varying the oscillator damping γ_0 . High and low damping values, $\gamma_0 \gg \gamma$ and $\gamma_0 \ll \gamma$, favor synchronization and lasing, respectively. In both cases the instability towards collective dynamics can occur not only on the resonance $\omega_B \approx \omega_0$ but also away from it in a relatively wide range of E fields, $\omega_B < \omega_0$ for synchronization and $\omega_B > \omega_0$ for lasing (see [37]). We note that the lasing regime can also be understood in terms of a negative AC conductivity that enables gain of THz radiation[5, 11–13].

An intriguing question for future work is the role of electron interactions. Several interesting regimes can be envisioned depending on the relation between carrier concentration and the localization radius of WS states $r_0 \sim J/eE$. At high carrier concentration, $nr_0^2 \gg 1$, the interactions will act to dephase the oscillations, producing an asynchronous Bloch-oscillating electron gas. To the contrary, at low carrier concentration, $nr_0^2 \ll 1$, the interactions will tend to create a spatially ordered Wigner solid of localized Bloch-oscillating carriers. Ordering will stabilize oscillations and facilitate synchronization.

Another question of interest is the effect of thermal fluctuations and noise. While the electron temperature

under a strong direct current is expected to be high, in the architecture considered above the temperature of an external oscillator is naturally decoupled from that of electrons. The oscillator will remain cold and provide a synchronizing feedback on the electron subsystem.

In summary, the unique electronic properties of the flat bands in moiré graphene, such as the bandwidth considerably narrower than the optical phonon energy, the ~ 10 nm-large superlattice periodicity and relatively high mobility, will facilitate observing the Bloch oscillations. The two-dimensional nature of the system offers addi-

tional benefits: the carriers, which are fully exposed, can be coupled to a nearby oscillator mode that will synchronize their movements to enable phase-coherent collective oscillations, a regime in which current-pumped synchronization and THz lasing can be realized and explored.

This work was supported by the Science and Technology Center for Integrated Quantum Materials, NSF Grant No. DMR-1231319; and Army Research Office Grant W911NF-18-1-0116 (L.L.). E.K. acknowledges financial support by the Research Travel Grant of the Karlsruhe House of Young Scientists (KHYS)

-
- [1] N. W. Ashcroft and N. D. Mermin, *Solid State Physics* (Saunders, Philadelphia, 1976).
 - [2] A. B. Pippard, *The Dynamics of Conduction Electrons* (Gordon and Breach Science Publishers, Inc., New York, 1965).
 - [3] L. Esaki and R. Tsu, Superlattice and Negative Differential Conductivity in Semiconductors, *IBM J. Res. Dev.*, **14**, 61-65 (1970).
 - [4] S. A. Kitorov, G. S. Simin, and V. Y. Sindalovskii, Bragg reflections and the high-frequency conductivity of an electronic solid-state plasma, *Fizika Tverdogo Tela*, **13**, 2230-2233 (1971) [*Soviet Physics - Solid State* **13**, 1872-1874 (1972)]
 - [5] H. Kroemer, On the nature of the negative-conductivity resonance in a superlattice Bloch oscillator, *arXiv:cond-mat/0007482* (2000).
 - [6] P. G. Savvidis, B. Kolasa, G. Lee, and S. J. Allen, Resonant Crossover of Terahertz Loss to the Gain of a Bloch oscillating InAs/AlSb Superlattice, *Phys. Rev. Lett.* **92**, 196802 (2004).
 - [7] A. Sibille, J. F. Palmier, H. Wang, and F. Molloy, Observation of Esaki-Tsu negative differential velocity in GaAs/AlAs superlattices, *Phys. Rev. Lett.* **64**, 52 (1990).
 - [8] J. Feldmann, K. Leo, J. Shah, D. A. B. Miller, J. E. Cunningham, T. Meier, G. von Plessen, A. Schulze, P. Thomas, and S. Schmitt-Rink, Optical investigation of Bloch oscillations in a semiconductor superlattice, *Phys. Rev. B* **46**, 7252 (1992).
 - [9] C. Waschke, H. G. Roskos, R. Schwedler, K. Leo, H. Kurz, and K. Kohler, Coherent submillimeter-wave emission from Bloch oscillations in a semiconductor superlattice, *Phys. Rev. Lett.* **70**, 3319 (1993).
 - [10] A. Rauh and G. H. Wannier, Theory of stark ladders in the optical absorption of solids, *Solid State Commun.* **15**, 1239 (1974).
 - [11] T. Hyart, K. N. Alekseev, and E. V. Thuneberg, Bloch gain in dc-ac-driven semiconductor superlattices in the absence of electric domains, *Phys. Rev. B* **77**, 165330 (2008).
 - [12] T. Hyart, N. V. Alexeeva, J. Mattas, and K. N. Alekseev, Terahertz Bloch Oscillator with a Modulated Bias, *Phys. Rev. Lett.* **102**, 140405 (2009).
 - [13] T. Hyart, J. Mattas, and K. N. Alekseev, Model of the Influence of an External Magnetic Field on the Gain of Terahertz Radiation from Semiconductor Superlattices, *Phys. Rev. Lett.* **103**, 117401 (2009).
 - [14] M. Ben Dahan, E. Peik, J. Reichel, Y. Castin, and C. Salomon, Bloch Oscillations of Atoms in an Optical Potential, *Phys. Rev. Lett.* **76**, 4508 (1996).
 - [15] B. P. Anderson, M. A. Kasevich, Macroscopic Quantum Interference from Atomic Tunnel Arrays, *Science* **282** (5394), 1686-1689 (1998).
 - [16] O. Morsch, J. H. Muller, M. Cristiani, D. Ciampini, and E. Arimondo, Bloch Oscillations and Mean-Field Effects of Bose-Einstein Condensates in 1D Optical Lattices, *Phys. Rev. Lett.* **87**, 140402 (2001).
 - [17] M. Cristiani, O. Morsch, J. H. Muller, D. Ciampini, and E. Arimondo, Experimental properties of Bose-Einstein condensates in one-dimensional optical lattices: Bloch oscillations, Landau-Zener tunneling, and mean-field effects, *Phys. Rev. A* **65**, 063612 (2002).
 - [18] H. Ott, E. de Mirandes, F. Ferlaino, G. Roati, G. Modugno, and M. Inguscio, Collisionally Induced Transport in Periodic Potentials, *Phys. Rev. Lett.* **92**, 160601 (2004).
 - [19] M. Gluck, F. Keck, A. R. Kolovsky, and H. J. Korsch, Wannier-Stark resonances in optical and semiconductor superlattices, *Phys. Reps.* **366** (3), 103-182 (2002).
 - [20] I. A. Dmitriev and R. A. Suris, Electron localization and bloch oscillations in quantum-dot superlattices under a constant electric field, *Semiconductors* **35**, 212 (2001).
 - [21] I. A. Dmitriev and R. A. Suris, Damping of Bloch oscillations in quantum dot superlattices: A general approach, *Semiconductors* **36**, 1364 (2002).
 - [22] A. R. Kolovsky, E. N. Bulgakov, Wannier-Stark states and Bloch oscillations in the honeycomb lattice, *Phys. Rev. A* **87** (3), 033602 (2013).
 - [23] R. Bistritzer and A. H. MacDonald, Moiré bands in twisted double-layer graphene. *Proc. Nat. Acad. Sci.* **108**, 12233-12237 (2011).
 - [24] Y. Cao, V. Fatemi, A. Demir, S. Fang, S. L. Tomarken, J. Y. Luo, J. D. Sanchez-Yamagishi, K. Watanabe, T. Taniguchi, E. Kaxiras, R. C. Ashoori, and P. Jarillo-Herrero, Correlated insulator behaviour at half-filling in magic-angle graphene superlattices. *Nature* **556**, 80-84 (2018).
 - [25] Y. Cao, V. Fatemi, S. Fang, K. Watanabe, T. Taniguchi, E. Kaxiras, and P. Jarillo-Herrero, Unconventional superconductivity in magic-angle graphene superlattices. *Nature* **556**, 43-50 (2018).
 - [26] Y. Cao, J. Y. Luo, V. Fatemi, S. Fang, J. D. Sanchez-Yamagishi, K. Watanabe, T. Taniguchi, E. Kaxiras, and P. Jarillo-Herrero, Superlattice-Induced Insulating States and Valley-Protected Orbits in Twisted Bilayer Graphene. *Phys. Rev. Lett.* **117**, 116804 (2016).
 - [27] Y. Kim, P. Herlinger, P. Moon, M. Koshino, T.

- Taniguchi, K. Watanabe and J. H. Smet, Charge Inversion and Topological Phase Transition at a Twist Angle Induced van Hove Singularity of Bilayer Graphene, *Nano Lett.* **16**, 5053-5059 (2016).
- [28] A. I. Berdyugin, B. Tsim, P. Kumaravadivel, S. G. Xu, A. Ceferino, A. Knothe, R. Krishna Kumar, T. Taniguchi, K. Watanabe, A. K. Geim, I. V. Grigorieva, V. I. Fal'ko, Minibands in twisted bilayer graphene probed by magnetic focusing, *Sci. Adv.* **6**: eaay7838 (2020)
 - [29] R. Bistritzer and A. H. MacDonald, Electronic cooling in graphene, *Phys. Rev. Lett.*, **102**, 206410 (2009).
 - [30] W. K. Tse, S. Das Sarma, Energy relaxation of hot Dirac fermions in graphene. *Phys. Rev. B.* **79**, 235406 (2009).
 - [31] J. C. W. Song, M. Y. Reizer, L. S. Levitov, Disorder-assisted electron-phonon scattering and cooling pathways in graphene. *Phys. Rev. Lett.* **109**, 106602 (2012).
 - [32] L. Ju, et al. Graphene plasmonics for tunable terahertz metamaterials. *Nat. Nanotechnol.* **6**, 630–643 (2011).
 - [33] H. Yan, et al. Tunable infrared plasmonic devices using graphene/insulator stacks. *Nat. Nanotechnol.* **7**, 330-334 (2012).
 - [34] H. Yan, et al. Infrared spectroscopy of tunable dirac terahertz magneto-plasmons in graphene. *Nano. Lett.* **12**, 3766-3771 (2012).
 - [35] N. H. Tu, K. Yoshioka, S. Sasaki, M. Takamura, K. Muraki and N. Kumada, Active spatial control of terahertz plasmons in graphene, *Communications Materials* **1**:7 (2020).
 - [36] L. Ateshian, H. Choi, M. Heuck, and D. Englund, Terahertz Light Sources by Electronic-Oscillator-Driven Second Harmonic Generation in Extreme-Confinement Cavities, *arXiv:2009.13029*
 - [37] See Supplementary Material for detailed estimates of phonon emission and carrier dephasing rates, and a step-by-step derivation of the backaction on the oscillator due to Bloch-oscillating carriers.

Supplemental Material

I. PHONON EMISSION RATES AND CARRIER DEPHASING

Here we consider carrier dephasing for Bloch-oscillating moiré superlattices due to phonon emission. Since the width of moiré bands is considerably smaller than the optical phonon energies, the electron-phonon interactions are dominated by coupling to acoustic phonons. We show that the acoustic phonon emission rates can be tuned in a wide range by two independent knobs—the width of the moiré band, controlled by the twist angle, and the in-plane electric field. The band-width impacts phonon emission through the density of states; phonon emission is suppressed when the twist angle is tuned away from the magic flat-band value. The electric field suppresses the emission rate by creating a discrete electron energy spectrum. As a result, phonon emission is suppressed as the field increases and the system enters the Bloch-oscillating state. Importantly, the threshold field for this suppression is relatively low, such that Bloch oscillations can be induced in the free-carrier regime, avoiding Wannier-Stark (WS) localization on a superlattice scale.

We start by writing down the full Hamiltonian, which contains the free-particle parts for electrons and phonons, and an electron-phonon interaction term, here taken in the deformation-potential form:

$$H = H_{\text{el}} + H_{\text{ph}} + H_{\text{el-ph}} \quad (\text{S1})$$

The electrons are described by a tight-binding model on a two-dimensional superlattice with a linear potential due to electric field:

$$H_{\text{el}} = - \sum_{\langle \mathbf{n}, \mathbf{n}' \rangle} J c_{\mathbf{n}}^\dagger c_{\mathbf{n}'} - \sum_{\mathbf{n}} e a \mathbf{E} \cdot \mathbf{n} c_{\mathbf{n}}^\dagger c_{\mathbf{n}} \quad (\text{S2})$$

where a is the superlattice period, $\mathbf{n} = (n_x, n_y)$ with integer n_x and n_y are the discrete coordinates that label the superlattice sites. Here, for simplicity, we model the superlattice as a square lattice. The electric field is applied along a general direction, the quantities $c_{\mathbf{n}}^\dagger$ and $c_{\mathbf{n}}$ are the creation and annihilation operators describing carriers on the lattice. Fermions in 2D continuum are described by superpositions of different Wannier orbitals,

$$\psi_{\mathbf{r}} = \sum_{\mathbf{n}} W(\mathbf{r} - \mathbf{n}a) c_{\mathbf{n}}, \quad \psi_{\mathbf{r}}^\dagger = \sum_{\mathbf{n}} W_{\mathbf{n}}^*(\mathbf{r} - \mathbf{n}a) c_{\mathbf{n}}^\dagger, \quad (\text{S3})$$

where $W(\mathbf{r} - \mathbf{n}a)$ are Wannier orbitals centered at the superlattice nodes.

Next we introduce the eigenstates of the electron Hamiltonian Eq.(S2), denoting them as $\phi_{\mathbf{n}}(\mathbf{r})$. As always for the WS ladder problem, the analysis is simplest in the momentum representation, $\phi_{\mathbf{n}}(\mathbf{r}) = \int d^2r e^{i\mathbf{p}\mathbf{r}} \phi_{\mathbf{n}}(\mathbf{p})$. Indeed, in momentum representation the Schroedinger

equation turns into a first-order ODE which can be solved explicitly. The states in the 2D continuum are then given by a convolution of the on-lattice states and Wannier orbitals, Eq.(S3).

Accordingly, carrying out the analysis yields the momentum-space wavefunctions $\phi_{\mathbf{n}}(\mathbf{p})$ given by products of the WS ladder wavefunctions $\Psi(\mathbf{n}, \mathbf{p})$ and the Wannier-orbital formfactors $W(\mathbf{p}) = \int d^2r e^{i\mathbf{p}\mathbf{r}} W(\mathbf{r})$:

$$\phi_{\mathbf{n}}(\mathbf{p}) = \Psi(\mathbf{n}, \mathbf{p}) W(\mathbf{p}) \quad (\text{S4})$$

Below, for simplicity, we use a Gaussian model for the quantities $W(\mathbf{p})$,

$$W(\mathbf{r}) = \frac{1}{\sqrt{\pi}\xi} e^{-\frac{r^2}{2\xi^2}}, \quad W(\mathbf{p}) = (2\pi)^{\frac{1}{2}} \xi e^{-p^2 \xi^2 / 2}. \quad (\text{S5})$$

where ξ defines the Wannier orbital radius. It will be convenient to factorize the Gaussian dependence as $W(\mathbf{p}) = w(p_x)w(p_y)$, where $\mathbf{p} = (p_x, p_y)$ and

$$w(p_j) = (2\pi)^{\frac{1}{4}} \xi^{\frac{1}{2}} e^{-p_j^2 \xi^2 / 2}, \quad j = x, y. \quad (\text{S6})$$

Importantly, the WS ladder wavefunction $\Psi(\mathbf{n}, \mathbf{p})$ can also be brought to a separable form for an electric field $\mathbf{E} = (E_x, E_y)$ applied in a generic incommensurate direction:

$$\Psi(\mathbf{n}, \mathbf{p}) = \psi_x(n_x, p_x) \psi_y(n_y, p_y), \quad (\text{S7})$$

with the factors $\psi_x(n_x, p_x)$ and $\psi_y(n_y, p_y)$ given by

$$\psi_j(n_j, p_j) = e^{-iF_{n_j}^{(i)}(p_j)}, \quad j = x, y \quad (\text{S8})$$

$$F_{n_j}^{(i)}(p_j) = \frac{2J}{eE_j a} \sin p_j a - n_j p_j a.$$

This yields a separable representation for the full momentum-space wavefunctions in Eq.(S4).

We note parenthetically that a more complicated treatment is required when an electric field is applied in a commensurate direction. In this case, instead of two-dimensional ladder, the WS problem yields a one-dimensional ladder, in which each level represents a one-dimensional band describing particle moving perpendicular to the electric field. Here, for simplicity, we focus on the case of the field applied in a generic incommensurate direction.

Next, we introduce phonons and electron phonon coupling. We model the acoustic phonons by the continuum Hamiltonian

$$H_{\text{ph}} = \int \frac{d^2q}{(2\pi)^2} \hbar \omega_{\mathbf{q}} a_{\mathbf{q}}^\dagger a_{\mathbf{q}}, \quad \omega_{\mathbf{q}} = s q \quad (\text{S9})$$

where s is the speed of sound, and the momenta \mathbf{q} form a continuum extending beyond the superlattice Brillouin zone. This model accounts for the presence of phonon modes with wavelengths that can be either shorter or greater than the superlattice periodicity a .

The electrons and phonons interact through the deformation potential coupling:

$$H_{\text{el-ph}} = \int d^2r D \nabla \cdot \mathbf{u}(\mathbf{r}) \psi_{\mathbf{r}}^\dagger \psi_{\mathbf{r}}, \quad (\text{S10})$$

$$u(\mathbf{r}) = \sum_k \sqrt{\frac{2\hbar}{\rho_0 \omega_k}} \left[a_k(t) e^{i\mathbf{k}\mathbf{r}} + a_k^\dagger(t) e^{-i\mathbf{k}\mathbf{r}} \right],$$

where ρ_0 is the atomic mass density, $a_k(t) = a_k e^{-i\omega_k t}$, $\psi_{\mathbf{r}}^\dagger$ and $\psi_{\mathbf{r}}$ are the creation and annihilation of an electron at a continuum position \mathbf{r} defined above.

To proceed with the analysis we rewrite the continuum electron-phonon coupling, Eq.(S10), in the basis of eigenstates found above, Eq.(S4). This gives

$$H_{\text{el-ph}} = \sum_{\mathbf{n}, \mathbf{n}'} \tilde{c}_{\mathbf{n}}^\dagger \tilde{c}_{\mathbf{n}'} \langle \mathbf{n} | D \nabla \cdot \mathbf{u} | \mathbf{n}' \rangle, \quad (\text{S11})$$

where $\tilde{c}_{\mathbf{n}}$ and $\tilde{c}_{\mathbf{n}}^\dagger$ denote fermion operators for the eigenstates in Eq.(S4), and $|\mathbf{n}\rangle$ is a short-hand notation for these states. Accordingly, the matrix element in Eq.(S11) equals

$$\langle \mathbf{n} | D \nabla \cdot \mathbf{u} | \mathbf{n}' \rangle = \int d^2r \phi_{\mathbf{n}}^*(\mathbf{r}) D \nabla \cdot \mathbf{u}(\mathbf{r}) \phi_{\mathbf{n}'}(\mathbf{r}). \quad (\text{S12})$$

Starting from the electron-phonon Hamiltonian Eq.(S11) and Fermi's golden rule, we express the phonon emission rate by a carrier transitioning from a state $|\mathbf{n}\rangle$ to a state $|\mathbf{n} - \mathbf{m}\rangle$ as

$$\gamma = \frac{2\pi}{\hbar} \frac{2D^2 \hbar}{\rho_0 s V} \sum_{\mathbf{m}}' \sum_{\mathbf{q}} |q| \left| \int d^2r e^{i\mathbf{q}\mathbf{r}} \bar{\phi}_{\mathbf{n}-\mathbf{m}}(\mathbf{r}) \phi_{\mathbf{n}}(\mathbf{r}) \right|^2 \delta(\hbar s |q| - e a \mathbf{m} \cdot \mathbf{E}) \quad (\text{S13})$$

where \mathbf{q} and $\hbar s |q|$ are the phonon momenta and energies, $\sum_{\mathbf{m}}'$ is the summation over all Bravais lattice vectors \mathbf{m} that satisfy the condition for phonon emission, $\mathbf{m} \cdot \mathbf{E} > 0$. Here we ignore phonon occupation numbers, assuming that electron temperature is much higher than the lattice temperature.

Next, we evaluate the matrix elements in Eq.(S13). In the general form given above the overlap integrals are pretty cumbersome. However the task of evaluating the overlap integrals can be simplified by employing an approximation of a small Wannier orbital radius, $\xi \ll a$. We start with plugging Eq.(S4)-(S9) into Eq.(S13),

$$\gamma = \frac{4\pi}{\hbar} \frac{D^2}{\rho_0 s^2} \sum_{\mathbf{m}}' \int \frac{|q| dq_x dq_y}{(2\pi)^2} \left| \sum_{p_x} \bar{\psi}_0 \left(p_x + \frac{q_x}{2} \right) \psi_{m_x} \left(p_x - \frac{q_x}{2} \right) \bar{w} \left(p_x + \frac{q_x}{2} \right) w \left(p_x - \frac{q_x}{2} \right) \right|^2 \times \left| \sum_{p_y} \dots \right|^2 \delta(|q| - Q_{\mathbf{m}}) \quad (\text{S14})$$

where

$$Q_{\mathbf{m}} = \frac{e a \mathbf{m} \cdot \mathbf{E}}{\hbar s} = \frac{e \pi \mathbf{m} \cdot \mathbf{E}}{\omega_*}, \quad \omega_* = \frac{\pi \hbar s}{a}, \quad (\text{S15})$$

is the emitted phonon momentum, ω_* is the superlattice Debye's frequency, and the quantity $|\sum_{p_y} \dots|^2$ is identical to $|\sum_{p_x} \dots|^2$ up to a replacement $p_x, q_x, E_x, m_x \rightarrow p_y, q_y, E_y, m_y$. Now, we evaluate the term $|\sum_{p_x} \dots|^2$ in this expression. Plugging Eq.(S8)-(S9) into Eq.(S14) yields

$$\left| \sum_{p_x} \dots \right|^2 = \left| \sum_{p_x} G(p_x) |w(p_x)|^2 \right|^2 e^{-q_x^2 \xi^2 / 2} \quad (\text{S16})$$

$$\approx |\langle G \rangle \sum_{p_x} |w(p_x)|^2|^2 e^{-q_x^2 \xi^2 / 2} = |\langle G \rangle|^2 e^{-q_x^2 \xi^2 / 2}$$

Here $G(p_x)$ denotes the function

$$e^{iF_0^{(x)}(p_x + q_x/2) - iF_{m_x}^{(x)}(p_x - q_x/2)} \quad (\text{S17})$$

which is periodic in p_x with the period $2\pi/a$. We evaluate the quantity in Eq.(S16) using that the period of $G(p_x)$ is much smaller than the width of $|w(p_x)|^2 = (2\pi)^{1/2} \xi e^{-\xi^2 p_x^2}$, namely $\pi/a \ll 1/\xi$. Accordingly, we replace $G(p_x)$ by its average value over the period and carried out integration over p_x as $\sum_{p_x} |w(p_x)|^2 = 1$. Evaluating the average $\langle G(p_x) \rangle = \frac{a}{2\pi} \int_{-\pi/a}^{\pi/a} dp_x G(p_x)$ gives a

Bessel function

$$\langle G(p_x) \rangle = e^{-im_x q_x a/2} J_{m_x} \left(\frac{4J \sin \left(\frac{q_x a}{2} \right)}{eE_x a} \right) \quad (\text{S18})$$

$$\gamma \sim \frac{4\pi}{\hbar} \frac{D^2}{\rho_0 s^2} \sum_{\mathbf{m}}' \int \frac{q^2 dq d\theta}{(2\pi)^2} \left| J_{m_x} \left(\frac{4J}{eE_x a} \sin \left(\frac{qa \cos \theta}{2} \right) \right) \right|^2 \left| J_{m_y} \left(\frac{4J}{eE_y a} \sin \left(\frac{qa \sin \theta}{2} \right) \right) \right|^2 e^{-q^2 \xi^2/2} \delta(|q| - Q_{\mathbf{m}}). \quad (\text{S19})$$

This expression, which was derived in the limit $a \gg \xi$, is reasonably accurate for the practically interesting parameter range $a \gtrsim \xi$.

The emission rate in Eq.(S19) shows an interesting behavior as a function of system parameters. Crucially, it is sharply suppressed when either the bandwidth J or the electric field E increases. These quantities can therefore serve as knobs to tune γ and thereby control the Bloch-oscillating carrier dephasing. The suppression of phonon emission in these two cases is governed by very different mechanisms. The impact of the bandwidth on γ can be understood in terms of the density of electronic states which control the emission rate, decreasing inversely with J . The dependence γ vs. E is fairly complicated due to the oscillatory character of the Bessel functions. The

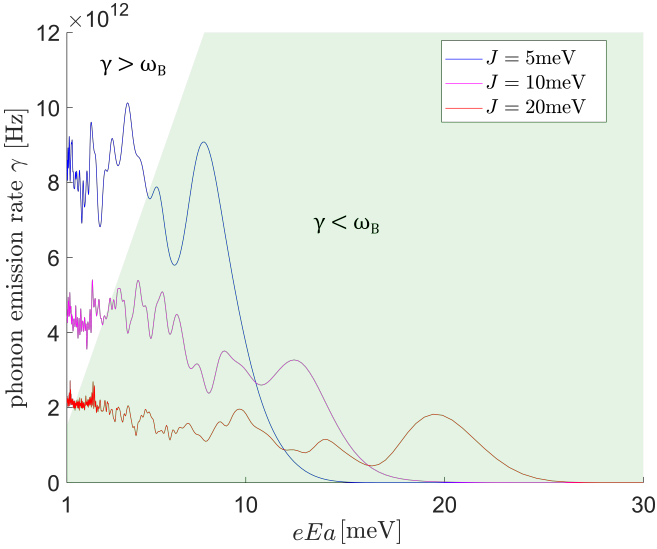


FIG. S1: The field dependence of phonon emission rate obtained from Eq.(S19) for several different bandwidth values, and typical moiré graphene parameter values given in the text. In the green shaded region the Bloch oscillations are underdamped, $\gamma < \omega_B = eEa/\hbar$; in the white region the oscillations are overdamped $\gamma > \omega_B$. The field orientation is incommensurate relative to the superlattice, such that $E_x/E_y = 1.618$. The suppression of emission rate under increasing bandwidth and growing electric field is a generic behavior expected to remain valid for other incommensurate electric field orientations.

Applying the same approach to the integral over p_y in Eq.(S14) yields a closed-form expression

general trend, however, is simple to understand by noting that the energy spacings in the two-dimensional WS ladder grow as E increases. As a result, the energies of different WS states are tuned out of resonance; this detuning suppresses phonon-mediated transitions. The suppression of phonon emission becomes exponential at E much larger than the threshold value set by the maximal energy of phonons emitted through this process, $eEa \gg \omega_{\max} \approx \omega_* \xi/a$.

We illustrate the suppression of γ in Fig.S1, which shows the emission rate obtained from Eq.(S19) for an electric field set to a generic direction. Numerical values for other quantities are chosen to mimic a MATBG bandstructure: the superlattice period $a = 10\text{nm}$, the Wannier function radius $\xi = 0.5a$. For these values, the superlattice Debye's frequency in Eq.(S15) is $\omega_* = 1\text{meV}$. For el-ph coupling we use the graphene monolayer deformation potential $D = 20\text{eV}$ and graphene mass density $\rho_0 = 7.6 \times 10^{-8}\text{g/cm}^2$.

The above analysis, carried out for a square lattice tight-binding model, predicts a behavior of phonon emission that we expect to remain qualitatively valid for other types of superlattices, in particular the moiré graphene superlattices. Namely, the large spatial periods of moiré superlattices and their abnormally narrow bandwidths limit phonon emission to the pathway dominated by acoustic phonons. We find, in particular, that the emission rate is quickly suppressed upon increasing the bandwidth, see Fig.S1. Since the moiré graphene bandwidth is highly sensitive to the twist angle, becoming small near the magic values, phonon emission can be suppressed by detuning the twist angle away from these values.

Likewise, the large superlattice periodicity results in a high sensitivity to the electric field. Our analysis predicts an abrupt quenching of phonon emission occurring already at moderate fields. The phonon emission rate features strong dependence on the bandwidth and field strength, these quantities can therefore serve as useful knobs allowing to realize and control Bloch oscillations.

II. THE BACKACTION ON THE OSCILLATOR DUE TO BLOCH-OSCILLATING CARRIERS AND THE ROLE OF OSCILLATOR DAMPING

Here we provide the details of the analysis of the back-action on the oscillator due to Bloch-oscillating carriers. We work with the equations of motion as given in Eqs.(8). We average over the randomness in the starting times t'_i ignoring the associated noise. This simple approach will be sufficient to understand the synchronization effect. The role of randomness and noise will be discussed elsewhere.

As a first step, we integrate Bloch dynamics of the i -th electron for times $t'_i < \tau < t$, which gives

$$\mathbf{p}_i(t) = e\mathbf{E}(t - t'_i) + \mathbf{p}_i(t'_i) + \alpha \int_{t'_i}^t Q(\tau') d\tau' \quad (\text{S20})$$

$$\mathbf{x}_i(t) = \mathbf{x}_i(t'_i) + \int_{t'_i}^t \mathbf{v}_i(\tau) d\tau,$$

where $\mathbf{v}_i(\tau) = \sum_l \frac{2J_l \mathbf{a}_l}{\hbar} \sin[\mathbf{a}_l \cdot \mathbf{p}(t)/\hbar]$. Averaging over the starting times t'_i must be carried out using the survival probability obeying the Poisson statistics $dp = dt\gamma e^{-\gamma(t-t'_i)}$.

It is instructive to first apply these relations to the free-carrier dynamics in the absence of coupling to the oscillator, $\alpha = 0$. In this case different carriers are totally decoupled and thus not synchronized. The drift velocity can be found by averaging $\mathbf{v}_i(t)$ as

$$\begin{aligned} \langle \mathbf{v}_i(t) \rangle &= \sum_{\mathbf{k}'} \int_{-\infty}^t dt' \gamma e^{-\gamma(t-t')} \mathbf{v}_i(t, t') \\ &= \sum_{\mathbf{k}'} \sum_l \frac{J_l \mathbf{a}_l}{i\hbar} \gamma \left[\frac{e^{i\mathbf{a}_l \cdot \mathbf{k}'}}{\gamma - i\frac{e}{\hbar} \mathbf{a}_l \cdot \mathbf{E}} - \frac{e^{-i\mathbf{a}_l \cdot \mathbf{k}'}}{\gamma + i\frac{e}{\hbar} \mathbf{a}_l \cdot \mathbf{E}} \right], \end{aligned} \quad (\text{S21})$$

where $\sum_{\mathbf{k}'}$ is a shorthand notation for averaging over the initial momentum distribution $\int \frac{d^2 k}{(2\pi)^2} f_0(\mathbf{k}')$ (here assumed to be steady-state). The quantity $\mathbf{v}_i(t, t')$ under the integral over t' is a sum of harmonics with frequencies ω_l , arising from the carrier velocity time dependence

$$\mathbf{v}_i(t, t') = \sum_l \frac{2J_l \mathbf{a}_l}{\hbar} \sin \left[\mathbf{a}_l \cdot \left(\frac{e}{\hbar} \mathbf{E}(t - t') + \mathbf{k}' \right) \right]. \quad (\text{S22})$$

Simplifying the result in Eq.S21 yields the drift velocity

$$\mathbf{v}_{\text{DC}} = \sum_{\mathbf{k}'} \sum_l \frac{2J_l \mathbf{a}_l}{\hbar} \cos(\mathbf{a}_l \cdot \mathbf{k}') \frac{\gamma \frac{e}{\hbar} \mathbf{a}_l \cdot \mathbf{E}}{\gamma^2 + (\frac{e}{\hbar} \mathbf{a}_l \cdot \mathbf{E})^2}. \quad (\text{S23})$$

Given by a sum of the terms $\frac{\gamma \omega_l}{\gamma^2 + \omega_l^2}$, the dependence v_{DC} vs. E is nonmonotonic, growing linearly at $E \lesssim E_\gamma = \gamma\hbar/ea$ and decreasing at $E \gtrsim E_\gamma$; at weak fields it matches the Drude theory prediction. The negative differential conductivity $dI/dV < 0$ is a testable signature of the Bloch-oscillation regime.

The spectrum of current fluctuations, Eq.(5), can be obtained in a similar manner. The velocity time dependence $\mathbf{v}_i(t, t')$ is a sum of harmonics with frequencies $\omega = \omega_l$; each harmonic producing a resonance broadened by the damping rate γ . Indeed, evaluating the Fourier components and averaging over the initial times gives

$$\int_{-\infty}^t dt' \gamma e^{-\gamma(t-t')} \mathbf{v}_i(t, t') e^{-i\omega(t-t')} \quad (\text{S24})$$

$$= \sum_l \frac{J_l \mathbf{a}_l}{i\hbar} \gamma \left[\frac{e^{i\mathbf{a}_l \cdot \mathbf{k}'}}{\gamma - i(\omega + \omega_l)} - \frac{e^{-i\mathbf{a}_l \cdot \mathbf{k}'}}{\gamma - i(\omega - \omega_l)} \right]. \quad (\text{S25})$$

Taking squares of the absolute values yields a fairly cumbersome expression for the noise spectrum. In the small- γ limit, achieved at $E \gtrsim E_\gamma$, it represents a comb of sharp Lorentzians plus a background part, see Eq.(5) and Fig.3.

Next, we reinstate the coupling to the oscillator and proceed with the analysis of synchronization. For conciseness, we focus on a resonance approximation valid near one of the resonances $\omega = \omega_l$ in Eq.(5), at $\omega_B \gg \gamma$. In what follows, without loss of generality, we take \mathbf{E} to be parallel to \mathbf{a}_l , and denote ω_l and \mathbf{a}_l as ω_B and a , respectively. Generalizing to the large- γ case and other field orientations will be straightforward. The special cases of field orientation such that $\mathbf{E} \cdot \mathbf{a}_l \approx \mathbf{E} \cdot \mathbf{a}_{l'}$, when two resonances can be excited simultaneously, will be discussed elsewhere.

The back-action of the carriers on the oscillator, given by the sum of carrier displacements $f(t) = \frac{\alpha}{m} \sum_i x_i(t)$ in Eq.9 averaged over the starting times t'_i with the Poissonian survival probability $dp = dt\gamma e^{-\gamma(t-t'_i)}$, equals

$$\begin{aligned} \langle x_i(t) \rangle &= \langle x_i(t') \rangle + \int_{-\infty}^t dt' \gamma e^{-\gamma(t-t')} \int_{t'}^t d\tau v_0 \sin \frac{ap_i(\tau)}{\hbar} \\ &= \int_{-\infty}^t dt' \gamma e^{-\gamma(t-t')} \int_{t'}^t d\tau v_0 \sin(\phi(\tau)), \quad v_0 = \frac{2aJ_l}{\hbar}, \end{aligned} \quad (\text{S26})$$

where we denote $\phi(\tau) = \omega_B(\tau - t') + \frac{\alpha a}{\hbar} \int_{t'}^\tau Q(\tau') d\tau'$. In what follows we drop the starting displacement term $\langle x_i(t') \rangle$, assuming that it vanishes under averaging as expected for a spatially uniform distribution.

The single mode dynamics is now described by Eq.(9) with the right-hand side replaced with a back-action memory function $\frac{\alpha}{m} N \langle x_i(t) \rangle$, where N is the number of Bloch electrons. We will consider the dynamics at lowest nonvanishing order in $Q(t)$, assuming the latter to be small. First, setting $Q(\tau') = 0$ and integrating over τ , we find $\langle x_i^{(0)}(t) \rangle = \frac{v_0 \omega_B}{\gamma^2 + \omega_B^2}$, a constant displacement that gives a time independent contribution to $f(t)$ in Eq.(9), which can be compensated for by shifting the oscillator equilibrium. Next, at first order in $Q(t)$, we Taylor-expand the sine term to obtain

$$\langle x_i^{(1)}(t) \rangle = \int_{-\infty}^t dt' \gamma e^{-\gamma(t-t')} \left(\int_{t'}^t d\tau v_0 \cos(\omega_B(\tau - t')) \left[\frac{\alpha a}{\hbar} \int_{t'}^{\tau} Q(\tau') d\tau' \right] \right). \quad (\text{S27})$$

Plugging in a harmonic dependence $Q(t) = Q_0 e^{-i\omega t}$, we evaluate the integrals over τ' and τ as

$$\begin{aligned} \int_{t'}^t d\tau v_0 \cos(\omega_B(\tau - t')) \left[\frac{\alpha a}{\hbar} \int_{t'}^{\tau} Q(\tau') d\tau' \right] &= \int_{t'}^t d\tau v_0 \cos(\omega_B(\tau - t')) \left[\frac{i\alpha a}{\hbar\omega} Q_0 (e^{-i\omega\tau} - e^{-i\omega t'}) \right] \\ &= \frac{i\alpha a v_0}{\hbar\omega} Q_0 \left(e^{-i\omega t} \frac{e^{i\omega_B(t-t')} - e^{i\omega(t-t')}}{2i(\omega_B - \omega)} + e^{-i\omega t'} \frac{e^{-i\omega_B(t-t')} - e^{i\omega(t-t')}}{-2i(\omega_B + \omega)} - e^{-i\omega t'} \frac{\sin \omega_B(t-t')}{\omega_B} \right). \end{aligned} \quad (\text{S28})$$

Integration over $t' < t$ in Eq.(S27) can now be carried out with the help of the identity

$$\int_{-\infty}^t dt' \gamma e^{-\gamma(t-t')} e^{-i\Omega(t-t')} = \frac{\gamma}{\gamma + i\Omega},$$

giving

$$\begin{aligned} \langle x_i^{(1)}(t) \rangle &= \frac{i\alpha a v_0}{\hbar\omega} Q_0 e^{-i\omega t} \left(\frac{\frac{\gamma}{\gamma - i\omega_B} - \frac{\gamma}{\gamma - i\omega}}{2i(\omega_B - \omega)} + \frac{\frac{\gamma}{\gamma + i\omega_B} - \frac{\gamma}{\gamma - i\omega}}{-2i(\omega_B + \omega)} - \frac{\frac{\gamma}{\gamma - i(\omega + \omega_B)} - \frac{\gamma}{\gamma - i(\omega - \omega_B)}}{2i\omega_B} \right) \\ &= \frac{i\alpha a v_0}{\hbar\omega} Q_0 e^{-i\omega t} \left(\frac{\gamma}{2(\gamma - i\omega_B)(\gamma - i\omega)} + \frac{\gamma}{2(\gamma + i\omega_B)(\gamma - i\omega)} - \frac{\gamma}{(\gamma - i(\omega + \omega_B))(\gamma - i(\omega - \omega_B))} \right) \\ &= \frac{i\alpha a v_0}{\hbar\omega} Q_0 e^{-i\omega t} \left(\frac{\gamma^2}{(\gamma^2 + \omega_B^2)(\gamma - i\omega)} + \frac{\gamma}{(\omega + i\gamma)^2 - \omega_B^2} \right). \end{aligned} \quad (\text{S29})$$

Substituting this result in Eq.(9) gives a characteristic equation for ω of the form given in Eq.(10). The instability criterion and the phase diagram for the oscillator damping equal to that of Bloch-oscillating carriers is discussed in the main text (see Fig.1 and accompanying discussion).

It is instructive to extend this analysis to the more general case of unequal damping rates for the oscillator and electrons, $\gamma_0 \neq \gamma$. After some algebra we arrive at the instability criterion

$$(\eta + 2(\gamma - \gamma_0)(\omega_B - \omega_0))^2 > \left((\omega_B - \omega_0)^2 + 4\gamma\gamma_0 \right) \times 4(\gamma + \gamma_0)^2. \quad (\text{S30})$$

A new interesting behavior found for $\gamma_0 \neq \gamma$ is an asymmetry between ω_B blue-shifted and red-shifted away from ω_0 , with the instability threshold lower for $\omega_B > \omega_0$ and higher for $\omega_B < \omega_0$ when $\gamma_0 < \gamma$, and vice versa when $\gamma_0 > \gamma$, as illustrated in Fig. S2. The asymmetry is particularly striking in the limit $\gamma_0/\gamma \rightarrow 0$: for $\omega_B > \omega_0$ the instability occurs at the coupling values η much smaller than those in Eq.(15), whereas for $\omega_B < \omega_0$ the instability threshold remains on the same order as in Eq.(15). Furthermore, perhaps somewhat counterintuitively, for

$\gamma_0/\gamma \rightarrow 0$ the lowest value of coupling at which the instability sets in occurs far away from the resonance $\omega_B = \omega_0$.

The origin of this asymmetry is closely related to the mechanism that enables the synchronized behavior. When the oscillator is undamped, synchronization arises due to the electrons pumping energy into the oscillator mode; subsequently, when this energy is passed back to electrons, they become synchronized with the oscillator, and with each other. However, at a weak coupling η , the energy transfer from the Bloch-oscillating electrons into the oscillator is possible only if $\hbar\omega_B > \hbar\omega_0$, indicating that the instability is easier to reach for ω_B values blue-shifted from ω_0 .

The above argument also suggests a reversal in the asymmetry when Bloch oscillations are weakly damped compared to the oscillator damping, $\gamma \ll \gamma_0$. Indeed, in this case it is the electron subsystem that serves as the main reservoir for energy storage, whereas the role of the oscillator mode is merely to lock the phases of different Bloch-oscillating carriers. Pumping energy into the collective mode now requires $\hbar\omega_B < \hbar\omega_0$. We therefore expect that in this limit the instability will occur at lower η values for ω_B red-shifted from ω_0 . This is exactly what Eq.(S30) predicts (see Fig.S2).

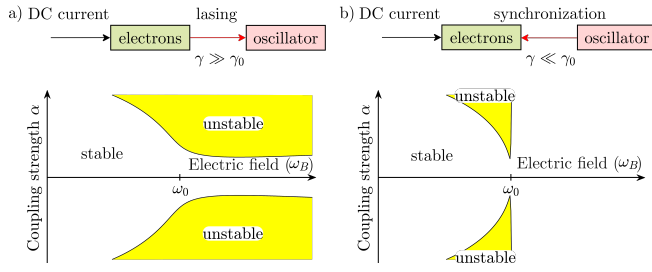


FIG. S2: The lasing and synchronization regimes. a) Lasing ($\gamma \gg \gamma_0$). In this case, the oscillator is weakly damped and serves as the main reservoir of the energy. Energy of the electrons is more easily pumped to the oscillator when $\omega_B > \omega_0$. Shown is the phase diagram for $\gamma = 100\gamma_0$. b) Synchronization ($\gamma \ll \gamma_0$). In this case, the oscillator is strongly damped and the electrons serve as the main reservoir of the energy. Energy of the oscillator is more easily pumped to the electrons when $\omega_B < \omega_0$. Shown is the phase diagram for $100\gamma = \gamma_0$. The instability criterion is a sign change of the imaginary parts of the roots of Eq. (11), which is negative in the stable regime and becomes positive in the unstable regime.